PHYSICAL REVIEW B **109**, 235407 (2024)

Magnetic topological insulators with switchable edge and corner states in monolayer VSi_2P_4

Xinming Wu, Zhiqi Chen, Yingxi Bai, Baibiao Huang, Ying Dai,[*] and Chengwang Niu[†]
School of Physics, State Key Laboratory of Crystal Materials, Shandong University, Jinan 250100, China

(Received 13 March 2024; accepted 29 May 2024; published 7 June 2024)

Magnetic topological insulators have been attracting great interest in two dimensions for both fundamental physics and applications in spintronics. Here, we put forward that the topological phase transition between a second-order topological insulator and quantum anomalous Hall insulator with a strikingly different bulk-boundary correspondence is possible in two-dimensional ferromagnets. We employ the intrinsic ferromagnetic VSi_2P_4 monolayer with giant valley polarization as a material candidate and elucidate that the second-order topological insulator emerges, distinguished by the topological indices $\chi^{(3)} = (-3, 2)$ and well-localized corner states. Remarkably, under strain engineering, a topological phase transition takes place under a 0.67% tensile strain accompanied by obtaining the quantum anomalous Hall effect with a Chern number $\mathcal{C} = -1$ and one chiral edge state. As the tensile strain further increases, another topological phase transition is realized as the VSi_2P_4 monolayer changes into a normal insulator. Our work considerably bridges the higher-order topology and quantum anomalous Hall effect with a high possibility of innovative applications in topotronic devices.

DOI: 10.1103/PhysRevB.109.235407

I. INTRODUCTION

Magnetic topological insulators (TIs) have currently stimulated significant interest with a variety of nontrivial phenomena being constantly discovered and intensively explored [1–4]. The Chern insulator (CI) with a fascinating quantum anomalous Hall (QAH) effect, in two-dimensional (2D) ferromagnets, has been a conceptual milestone with rich fundamental physics and great potential in the application of dissipationless spintronic devices [5–9]. With an integer Chern number $\mathcal{C}$, as a key desirable characteristic, the nontrivial topology of the QAH effect is distinguished by the $\mathcal{C}$ number of gapless chiral edge states in the corresponding one-dimensional nanoribbons. This is well known as bulk-boundary correspondence, i.e., a d-dimensional nontrivial insulator has nontrivial boundary states in $(d-1)$ dimensions [10–12].

Recently, the research on topological states has started to branch out to the generalized bulk-boundary correspondence [13–17]. For example, a d-dimensional second-order TI (SOTI) holds gapless states at the $(d-2)$-dimensional boundaries, but gapped states otherwise [18–21]. Indeed, recent years have witnessed an explosion of research investigating the complex interplay between SOTIs and magnetism [22,23]. For example, the topological phase transitions between topological crystalline insulators and SOTIs can be obtained via switching the magnetization directions in 3D $EuIn_2As_2$ [24] and 2D NpSb [25], and the 2D TIs and 2D SOTIs can be bridged by the in-plane Zeeman field [26,27] or by the ferroelectric switching [28]. However, only limited intrinsic 2D ferromagnets have been proposed theoretically to host the SOTI phase, and, moreover, the topological phase transitions between CIs and SOTIs remain elusive.

On the other hand, current research has witnessed a tremendous development in valleytronics, where valley polarization, as a new degree of freedom in honeycomb lattices, holds great opportunities for exotic transport phenomena [29–31]. In the present paper, we combine valley polarization and band topology to identify the manipulation of topological corner and edge states, accompanied by a topological phase transition between SOTI and CI, in a 2D VSi_2P_4 monolayer. Using first-principles calculations, we show that the VSi_2P_4 monolayer is an intrinsic ferromagnetic (FM) SOTI characterized by the emergence of nontrivial corner states. Moreover, spontaneous valley polarization emerges due to the coexistence of spin-orbit coupling (SOC) effects and exchange interactions of the localized d electrons. Consequently, the gap closure can be achieved at $+K$ and $-K$ sequentially, leading to the topological phase transitions from a FM SOTI to a CI and then to a normal insulator under tensile strain. The obtained QAH effect is distinguished by a nonzero Chern number $\mathcal{C} = -1$ and one chiral edge state. Our predicted topological phase transitions are helpful and essential for both the fundamental understanding and future applications of magnetic topological states with different bulk-boundary correspondences.

II. COMPUTATIONAL DETAILS

First-principles calculations are carried out by means of density functional theory (DFT) using the projector augmented-wave method as implemented in the Vienna *ab initio* simulation package (VASP) [32,33]. The generalized gradient approximation (GGA) within the Perdew-Burke-Ernzerhof (PBE) is used for the exchange-correlation potential [34]. The cutoff energy is fixed to 500 eV for the plane-wave basis set, and a vacuum layer of 20 Å is used

---

[*] Contact author: daiy60@sdu.edu.cn
[†] Contact author: c.niu@sdu.edu.cn

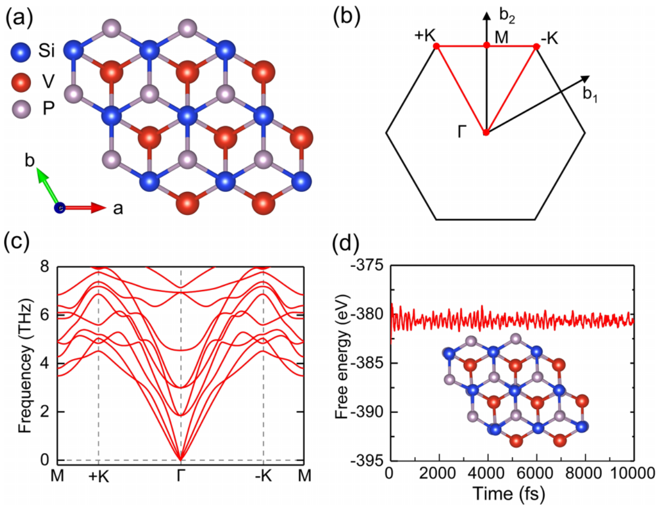

FIG. 1. (a) Top view of the crystal structure of the VSi_2P_4 monolayer. (b) The first Brillouin zone with marked high-symmetry points. Here, b_1 and b_2 are reciprocal lattice vectors. (c) The phonon dispersion and (d) time evolution of free energy during the molecular dynamics calculations for the VSi_2P_4 monolayer, showing that the monolayer is dynamically and thermally stable.

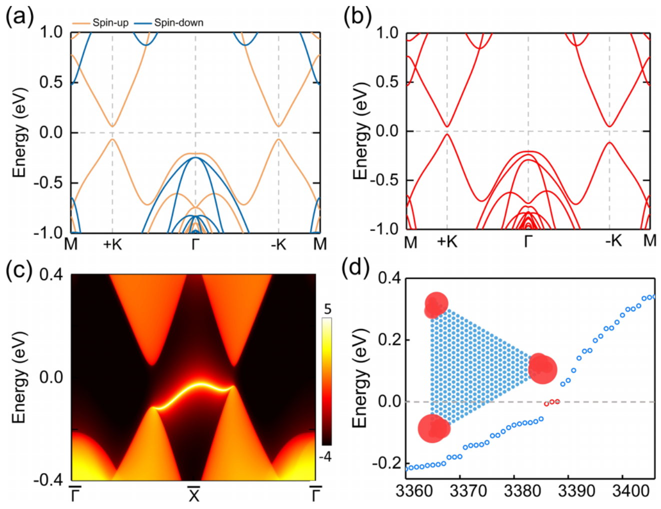

FIG. 2. Band structures of the VSi_2P_4 monolayer (a) without and (b) with SOC. (c) The gapped edge state of a VSi_2P_4 semi-infinite ribbon with an armchair edge. (d) Energy spectrum of a triangular armchair nanoflake for the VSi_2P_4 monolayer, where the occupied corner states are marked by red dots. The insets show the total charge distribution of the three corner states.

to avoid interactions between the nearest slabs. The strong correlation effects for V-3d electrons are handled via the GGA+U method with a value of $U = 2.4$ eV [35]. All atoms are completely relaxed until the atomic forces on each atom are smaller than 0.01 eV/Å, and the criterion for energy convergence is set to 10^{-6} eV. The Γ-centered Monkhorst-Pack grids of $9 \times 9 \times 1$ are employed to perform the first Brillouin zone integral. Using the DFT perturbation theory, the phonon calculations are carried out by using the PHONOPY package [36]. Maximally localized Wannier functions (MLWFs), combining the results of first-principles calculations of VASP, are constructed in the basis of V-d, Si-p, and P-p by using the WANNIER90 code [37].

III. RESULTS AND DISCUSSION

As illustrated in Fig. 1(a), the VSi_2P_4 monolayer exhibits a hexagonal lattice with space group $P\bar{6}m2$, forming on a hexagonal lattice. It consists of one V, two Si, and four P atoms in each unit cell, stacking in a sequence of P-Si-P-V-P-Si-P. Its optimized lattice constant is $a = 3.485$ Å, agreeing well with previous theoretical values [38,39]. In order to confirm the dynamical stability of the VSi_2P_4 monolayer, the phonon spectrum calculations are carried out. As shown in Fig. 1(c), the absence of imaginary modes in the entire Brillouin zone confirms that the VSi_2P_4 is dynamically stable and difficult to destroy once formed. Moreover, the molecular dynamics simulations are carried out for 10 ps at 300 K. As illustrated in Fig. 1(d), there is neither bond breakage nor structure reconstruction, suggesting a robust thermal stability for VSi_2P_4.

Each V atom is coordinated with six P atoms, forming a trigonal prismatic configuration and leading to the V-3d splitting into three groups: $a_1(d_{z^2})$, $e_1(d_{xy}, d_{x^2-y^2})$, and $e_2(d_{xz}, d_{yz})$. The valence electronic configuration of an isolated V atom is $3d^3 4s^2$, and, for VSi_2P_4, each V atom transfers four electrons to neighboring P atoms, i.e., the V^{4+} in VSi_2P_4 has one valence electron left and thus a magnetic moment of $1\mu_B$ is expected. This is further verified by our calculations with the results revealing that VSi_2P_4 is spin polarized and a magnetic moment of $1\mu_B$ per unit cell is indeed obtained. To determine the magnetic ground state, we investigate the total energies of VSi_2P_4 with FM and antiferromagnetic (AFM) configurations based on a $2 \times 2 \times 1$ supercell. The FM configuration is found to be the magnetic ground state, which is energetically favored over the AFM ones by 57.2 meV per V, and this large value indicates that the FM coupling is strong and robust in VSi_2P_4. Indeed, the FM ground state can be understood by the Goodenough-Kanamori rules because the V-P-V angles approach 90°, which are measured to be 91.71° [40,41]. After including the SOC effect, the magnetic anisotropy energy (MAE) was also calculated, and the out-of-plane direction is calculated to be the most energetically stable.

Figure 2(a) presents the band structures of VSi_2P_4 in the absence of SOC. It is clearly visible that the bands of opposite spins split significantly with only the spin-up bands left around the Fermi level. The VSi_2P_4 is a direct-gap insulator with an energy gap of 128.6 meV, where both the conduction band minimum (CBM) and valence band maximum (VBM) are located at the $\pm K$ points, and there is no valley polarization. When SOC is switched on, as shown in Fig. 2(b), the insulating character is maintained with a decrease of the band gap to 76.2 meV. The valley degeneracy in VSi_2P_4 at the $\pm K$ points is lifted obviously, meaning that spontaneous valley polarization is realized. Remarkably, the valley polarization in the top valence band can reach as much as 84.2 meV, which is relatively large compared to previously proposed ferrovalley systems [42,43], which is highly desirable for both fundamental physics and future applications in valleytronics.

The highest occupied bands around the $\pm K$ points are mainly contributed by the V-$d_{xy}/d_{x^2-y^2}$ orbitals, as illustrated

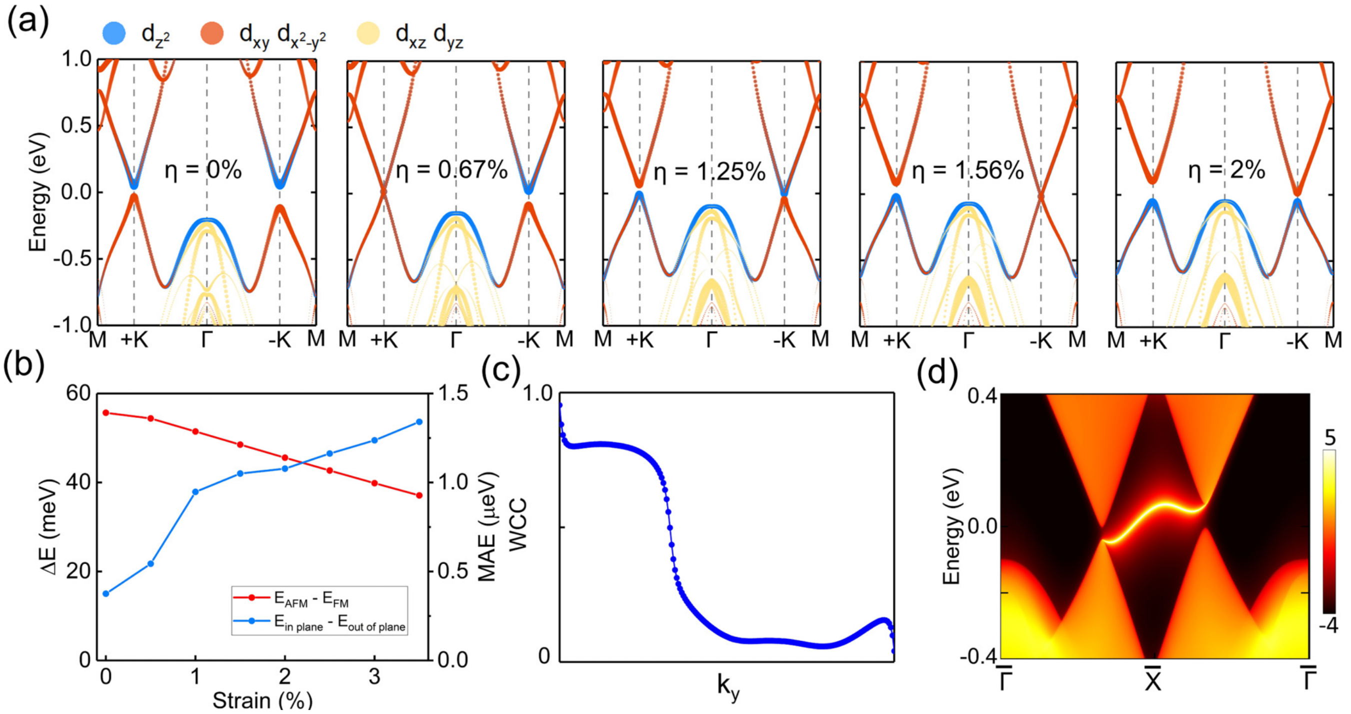

FIG. 3. (a) Orbitally resolved band structures of the VSi$_2$P$_4$ monolayer with SOC under different tensile strains, weighted with the V-d_{z^2}, V-$d_{xy}/d_{x^2-y^2}$, and V-d_{xz}/d_{yz} orbitals. Band inversions occur at the $+K$ and $-K$ valleys sequentially. (b) The energy differences ΔE between FM and AFM states and the MAE with respect to the tensile strains. (c) Evolution of WCC and (d) chiral edge state of a semi-infinite ribbon for the VSi$_2$P$_4$ monolayer under 1.25% tensile strain, demonstrating the quantum anomalous Hall effect with $\mathcal{C} = -1$.

in Fig. 3(a), while the lowest unoccupied bands are dominated by the V-d_{z^2} orbitals. Thus, the basis functions can be written as $|\psi_v^\tau\rangle = \sqrt{\frac{1}{2}}(|d_{x^2-y^2}\rangle + i\tau|d_{xy}\rangle)$ and $|\psi_c^\tau\rangle = |d_{z^2}\rangle$, respectively, and energy levels are given as $E_v^\tau = \langle\psi_v^\tau|\hat{H}_{\rm SOC}^0|\psi_v^\tau\rangle$ and $E_v^\tau = \langle\psi_c^\tau|\hat{H}_{\rm SOC}^0|\psi_c^\tau\rangle$. Here, c and v represent the conduction and valence bands, and τ refers to the valley index. Under the out-of-plane FM ground state, $\hat{H}_{\rm SOC}^0$ can be expressed as $\hat{H}_{\rm SOC}^0 = \lambda\hat{S}_{z'}\hat{L}_z = \alpha\hat{L}_z$. Thus the valley polarizations in the conduction and valence bands are $E_c^+ - E_c^- = 0$ and $E_v^+ - E_v^- = -4\alpha$, agreeing well with our calculated results that the valley degeneracy is removed in the top valence band.

We are most interested in the topological properties of the VSi$_2$P$_4$ monolayer. The band analysis reveals that there is no SOC-induced band inversion, which is one of the most obvious features of conventional TIs. Then, we perform calculations of the edge states of VSi$_2$P$_4$ using the MLWFs that can reproduce the band dispersion very well. Figure 2(d) displays the edge state of the VSi$_2$P$_4$ monolayer along the armchair boundary, and an obvious band gap can be noticed clearly, that is to say, the VSi$_2$P$_4$ monolayer is not a conventional 2D first-order TI. Then, we construct a triangular nanoflake along the armchair boundaries via the MLWFs, and analyze the corner states [44], which are the hallmark of 2D SOTIs. As illustrated in Fig. 2(c), three continuous states (red dots) around the Fermi level in the gap can be observed, and remarkably their spatial distribution is well localized at the corners of the nanoflake, revealing the emergence of corner states of the SOTI phase.

To provide conclusive proof of the SOTI state for the VSi$_2$P$_4$ monolayer, we calculate the topological indices $\chi^{(3)} = \{[K_1^{(3)}], [K_2^{(3)}]\}$ and the fractional charges $Q_c = \frac{2}{3}([K_1^{(3)}] + [K_2^{(3)}]) \bmod 2e$. $[K_1^{(3)}], [K_2^{(3)}]$ are given by comparing the number of C_3 rotation symmetry eigenvalues of the occupied bands between the K and Γ points, where the spinful eigenvalues of the C_3 rotation symmetry are $\{e^{i\pi/3}, -1, e^{-i\pi/3}\}$. The calculated topological indices $\chi^{(3)} = (-3, 2)$ and the fractional charge is $Q_c = \frac{4}{3}$, confirming the SOTI nature of the VSi$_2$P$_4$ monolayer.

Now, we turn to the topological phase transition that provides further insight into both the fundamental understanding and the potential use of topological states [45,46]. It is well known that the strain engineering is an effective strategy for tuning the electronic, magnetic, and topological properties of 2D materials [47,48]. The strain strength is defined as $\eta = (a - a_0)/a_0 \times 100\%$, where a and a_0 represent the lattice parameters of the VSi$_2$P$_4$ monolayer with and without strain. Because the compressive strain does not influence the topological phase transition, the following analyses are only focused on the tensile strain. Figure 3(b) displays the exchange energy differences of the FM and AFM configurations as a function of strain. Although the differences between the energies of the FM and AFM states are decreasing, the FM states are always the magnetic ground states for the VSi$_2$P$_4$ monolayer. Moreover, we also investigate the changes of MAE under the tensile strain, and the results are also presented in Fig. 4(b). We find that the MAE of the VSi$_2$P$_4$ monolayer will increase with growing strain, and

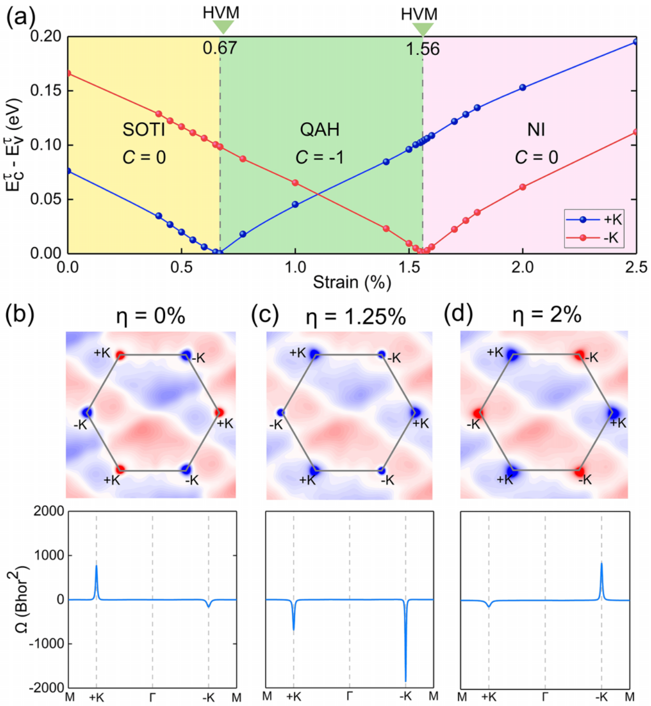

FIG. 4. (a) Variation of the energy gaps at the $+K$ and $-K$ valleys and the phase diagram for the $\mathrm{VSi_2P_4}$ monolayer with respect to tensile strains. K-space distributions of Berry curvatures and/or that along the high-symmetry points for the $\mathrm{VSi_2P_4}$ monolayer under tensile strains of (b) 0%, (c) 1.25%, and (d) 2%, respectively.

will always maintain a positive value, which means that the magnetic easy axis of the $\mathrm{VSi_2P_4}$ monolayer is robust out of plane under strain. That is to say, the magnetic ground state would be maintained under the changes of tensile strains from 0% to 3.5%.

To get preliminary insight into the topological phase transition, we present in Fig. 4(a) the calculated energy gaps of FM $\mathrm{VSi_2P_4}$ at valleys $\pm K$ as a function of tensile strain η. Indeed, the band gaps as well as the band topology can be effectively modified by the tensile strain. The band gap decreases with the tensile strain increasing at both $\pm K$, and the band at $+K$ becomes gapless under the strain of 0.67% while that at $-K$ remains open, i.e., $\mathrm{VSi_2P_4}$ becomes a half-valley metal. Across this critical strain, the band gap at $+K$ reopens. Remarkably, the process of the band gap closing and reopening is generally accepted as the heuristic scenario of a topological phase transition. Moreover, while the orbital contributions at $-K$ remain the same as its equilibrium lattice, the band inversion occurs at the $+K$ valley, as shown in Fig. 3(a), suggesting further the strain-induced topological phase transition in the $\mathrm{VSi_2P_4}$ monolayer.

To determine the band topology of the obtained 2D FM insulators, taking $\eta = 1.25\%$ as an example, we calculate the anomalous Hall conductivity, given by $\sigma_{xy}^A = \mathcal{C}e^2/h$, where $\mathcal{C}$ is the Chern number that can be obtained by $\mathcal{C} = \frac{1}{2\pi}\int_{\mathrm{BZ}} \Omega(\mathbf{k}) d^2k$ and $\Omega(\mathbf{k})$ is the Berry curvature over all of the occupied states [49,50],

$$\Omega(\mathbf{k}) = \sum_{n<E_F}\sum_{m\neq n} 2\,\mathrm{Im}\frac{\langle\psi_{n\mathbf{k}}|\upsilon_x|\psi_{m\mathbf{k}}\rangle\langle\psi_{m\mathbf{k}}|\upsilon_y|\psi_{n\mathbf{k}}\rangle}{(\varepsilon_{m\mathbf{k}}-\varepsilon_{n\mathbf{k}})^2}, \quad (1)$$

where m, n are band indices, $\psi_{m/n\mathbf{k}}$ and $\varepsilon_{m/n\mathbf{k}}$ are the Bloch wave functions and corresponding eigenenergies of band m/n, respectively, and $\upsilon_{x/y}$ are the velocity operators. When the chemical potential is located within the insulating region, the quantization of σ_{xy}^A with $\mathcal{C} = -1$, which arises mainly from the Berry curvature $\Omega(\mathbf{k})$ around the $\pm K$ valleys as illustrated in Fig. 4(c), can indeed be obtained. We also employ the Wilson loop method to confirm the nonzero Chern number shown in Fig. 3(c). In addition, the edge states are calculated via using the MLWFs. As shown in Fig. 3(d), a single chiral edge state crosses the Fermi level and connects the valence and conduction bands, demonstrating the QAH effect in $\mathrm{VSi_2P_4}$ under a 1.25% tensile strain, i.e., a topological phase transition from the SOTI to QAH insulator occurs.

As the tensile strain η further increases, the energy gaps at the $+K$ valley continue to increase linearly, and notably, around $\eta = 1.56\%$, energy gaps at the $-K$ valley experience the process of closing and reopening as well. After that, the valley polarization is gradually switched from the top valence band to the bottom conduction band with $E_v^+ - E_v^- = 0$ and $E_c^+ - E_c^- = -4\alpha$. This is due to the fact that band inversion occurs also at the $-K$ valley, as illustrated in Fig. 3(a), leading to the lowest unoccupied bands being dominated by the V-$d_{xy}/d_{x^2-y^2}$ orbitals at both the $+K$ and $-K$ valleys while the highest occupied bands are dominated by the V-d_{z^2} orbitals. The sign of the Berry curvature $\Omega(\mathbf{k})$ around $-K$ flips, as shown in Fig. 4(d), and the Chern number becomes to $\mathcal{C} = 0$. Therefore, another topological phase transition is realized as the $\mathrm{VSi_2P_4}$ monolayer changes from a CI to a normal insulator with the chiral edge states disappearing.

IV. CONCLUSIONS

In summary, we have demonstrated the $\mathrm{VSi_2P_4}$ monolayer is a 2D FM SOTI, and, remarkably, topological phase transitions from a SOTI to a QAHI and then to a normal insulator can be obtained with strain-engineered valleys. The magnetic ground state has been predicted to remain energetically stable under tensile strain. At tensile strain strengths larger than 0.67%, the FM $\mathrm{VSi_2P_4}$ changes from the SOTI to CI with an integer Chern number of $\mathcal{C} = -1$, and at tensile strain strengths greater than 1.56%, it becomes a normal insulator. The topological natures of SOTI and CI are further validated through the emergence of nontrivial corner states and chiral edge states, respectively. Our results not only enrich the candidates of 2D magnetic SOTIs and CIs, but also offer a platform for investigating the relationship among magnetic topological states in two dimensions [44].

ACKNOWLEDGMENTS

This work was supported by the National Natural Science Foundation of China (Grants No. 12174220 and No. 12074217), the Shandong Provincial Science Foundation for Excellent Young Scholars (Grant No. ZR2023YQ001), the Taishan Young Scholar Program of Shandong Province, and the Qilu Young Scholar Program of Shandong University.

[1] Y. Tokura, K. Yasuda, and A. Tsukazaki, Nat. Rev. Phys. **1**, 126 (2019).

[2] J. Xiao and B. Yan, Nat. Rev. Phys. **3**, 283 (2021).

[3] F. Islam, Y. Lee, D. M. Pajerowski, J. Oh, W. Tian, L. Zhou, J. Yan, L. Ke, R. J. McQueeney, and D. Vaknin, Adv. Mater. **35**, 2209951 (2023).

[4] X. Wang, X.-P. Li, J. Li, C. Xie, J. Wang, H. Yuan, W. Wang, Z. Cheng, Z.-M. Yu, and G. Zhang, Adv. Funct. Mater. **33**, 2304499 (2023).

[5] H. Weng, R. Yu, X. Hu, X. Dai, and Z. Fang, Adv. Phys. **64**, 227 (2015).

[6] Y. Ren, Z. Qiao, and Q. Niu, Rep. Prog. Phys **79**, 066501 (2016).

[7] C.-Z. Chang, C.-X. Liu, and A. H. MacDonald, Rev. Mod. Phys. **95**, 011002 (2023).

[8] X. Wu, R. Li, X. Zou, B. Huang, Y. Dai, and C. Niu, Phys. Rev. B **108**, 115438 (2023).

[9] J. Zeng, T. Hou, Z. Qiao, and W.-K. Tse, Phys. Rev. B **100**, 205408 (2019).

[10] M. Z. Hasan and C. L. Kane, Rev. Mod. Phys. **82**, 3045 (2010).

[11] X.-L. Qi and S.-C. Zhang, Rev. Mod. Phys. **83**, 1057 (2011).

[12] A. Bansil, H. Lin, and T. Das, Rev. Mod. Phys. **88**, 021004 (2016).

[13] W. A. Benalcazar, B. A. Bernevig, and T. L. Hughes, Science **357**, 61 (2017).

[14] F. Schindler, A. M. Cook, M. G. Vergniory, Z. Wang, S. S. P. Parkin, B. A. Bernevig, and T. Neupert, Sci. Adv. **4**, eaat0346 (2018).

[15] B. Xie, H.-X. Wang, X. Zhang, P. Zhan, J.-H. Jiang, M. Lu, and Y. Chen, Nat. Rev. Phys. **3**, 520 (2021).

[16] Y. Bai, N. Mao, R. Li, Y. Dai, B. Huang, and C. Niu, Small **19**, 2206574 (2023).

[17] C.-A. Li, S.-B. Zhang, J. Li, and B. Trauzettel, Phys. Rev. Lett. **127**, 026803 (2021).

[18] B. Liu, G. Zhao, Z. Liu, and Z. F. Wang, Nano Lett. **19**, 6492 (2019).

[19] X.-L. Sheng, C. Chen, H. Liu, Z. Chen, Z.-M. Yu, Y. X. Zhao, and S. A. Yang, Phys. Rev. Lett. **123**, 256402 (2019).

[20] Z. Wang, B. J. Wieder, J. Li, B. Yan, and B. A. Bernevig, Phys. Rev. Lett. **123**, 186401 (2019).

[21] J.-H. Wang, Y.-B. Yang, N. Dai, and Y. Xu, Phys. Rev. Lett. **126**, 206404 (2021).

[22] H. Mu, G. Zhao, H. Zhang, and Z. Wang, npj Comput. Mater. **8**, 82 (2022).

[23] M. Ezawa, Phys. Rev. B **97**, 155305 (2018).

[24] Y. Xu, Z. Song, Z. Wang, H. Weng, and X. Dai, Phys. Rev. Lett. **122**, 256402 (2019).

[25] N. Mao, X. Hu, H. Wang, Y. Dai, B. Huang, Y. Mokrousov, and C. Niu, Phys. Rev. B **103**, 195152 (2021).

[26] Y. Ren, Z. Qiao, and Q. Niu, Phys. Rev. Lett. **124**, 166804 (2020).

[27] C. Chen, Z. Song, J.-Z. Zhao, Z. Chen, Z.-M. Yu, X.-L. Sheng, and S. A. Yang, Phys. Rev. Lett. **125**, 056402 (2020).

[28] R. Li, N. Mao, L. Cai, Y. Bai, B. Huang, Y. Dai, and C. Niu, Phys. Rev. B **108**, 125302 (2023).

[29] D. Xiao, W. Yao, and Q. Niu, Phys. Rev. Lett. **99**, 236809 (2007).

[30] M. Sui, G. Chen, L. Ma, W.-Y. Shan, D. Tian, K. Watanabe, T. Taniguchi, X. Jin, W. Yao, D. Xiao, and Y. Zhang, Nat. Phys. **11**, 1027 (2015).

[31] Z. Chen, R. Li, Y. Bai, N. Mao, M. Zeer, D. Go, Y. Dai, B. Huang, Y. Mokrousov, and C. Niu, Nano Lett. **24**, 4826 (2024).

[32] G. Kresse and J. Hafner, Phys. Rev. B **47**, 558 (1993).

[33] G. Kresse and J. Furthmüller, Phys. Rev. B **54**, 11169 (1996).

[34] J. P. Perdew, K. Burke, and M. Ernzerhof, Phys. Rev. Lett. **77**, 3865 (1996).

[35] S. L. Dudarev, G. A. Botton, S. Y. Savrasov, C. J. Humphreys, and A. P. Sutton, Phys. Rev. B **57**, 1505 (1998).

[36] A. Togo and I. Tanaka, Scr. Mater. **108**, 1 (2015).

[37] F. Freimuth, Y. Mokrousov, D. Wortmann, S. Heinze, and S. Blügel, Phys. Rev. B **78**, 035120 (2008).

[38] S.-D. Guo, W.-Q. Mu, Y.-T. Zhu, and X.-Q. Chen, Phys. Chem. Chem. Phys. **22**, 28359 (2020).

[39] Y.-L. Hong, Z. Liu, L. Wang, T. Zhou, W. Ma, C. Xu, S. Feng, L. Chen, M.-L. Chen, D.-M. Sun, X.-Q. Chen, H.-M. Cheng, and W. Ren, Science **369**, 670 (2020).

[40] J. B. Goodenough, Phys. Rev. **100**, 564 (1955).

[41] J. Kanamori, J. Phys. Chem. Solids **10**, 87 (1959).

[42] X. Li, T. Cao, Q. Niu, J. Shi, and J. Feng, Proc. Natl. Acad. Sci. USA **110**, 3738 (2013).

[43] P. Zhao, Y. Ma, C. Lei, H. Wang, B. Huang, and Y. Dai, Appl. Phys. Lett. **115**, 261605 (2019).

[44] See Supplemental Material at http://link.aps.org/supplemental/10.1103/PhysRevB.109.235407 for complete Monte Carlo simulations, and energy spectra of the finite nanoflakes.

[45] S.-Y. Xu, Y. Xia, L. A. Wray, S. Jia, F. Meier, J. H. Dil, J. Osterwalder, B. Slomski, A. Bansil, H. Lin, R. J. Cava, and M. Z. Hasan, Science **332**, 560 (2011).

[46] C. Niu, J.-P. Hanke, P. M. Buhl, H. Zhang, L. Plucinski, D. Wortmann, S. Blügel, G. Bihlmayer, and Y. Mokrousov, Nat. Commun. **10**, 3179 (2019).

[47] C. Niu, P. M. Buhl, G. Bihlmayer, D. Wortmann, S. Blügel, and Y. Mokrousov, Nano Lett. **15**, 6071 (2015).

[48] X. Feng, L. Cai, Z. Chen, Y. Dai, B. Huang, and C. Niu, Appl. Phys. Lett. **122**, 193104 (2023).

[49] D. J. Thouless, M. Kohmoto, M. P. Nightingale, and M. den Nijs, Phys. Rev. Lett. **49**, 405 (1982).

[50] Y. Yao and Z. Fang, Phys. Rev. Lett. **95**, 156601 (2005).